Camera-based Vibration Measurement of the Portsmouth, NH WWI Memorial Bridge

Justin G. Chen [1]

Travis M. Adams [2]

Hao Sun [3]

Erin S. Bell, M.ASCE [4]

Oral Büyüköztürk [5]

ABSTRACT

Structural health monitoring (SHM) is a method for determining the structural integrity of civil infrastructure elements as a basis for maintenance and repair protocols. This monitoring depends on collecting structural response data from sensors installed on the structure due to in-service excitations. The installation additionally requires access to structural elements, power, and communication. New methods for remote measurement of displacements using video cameras could greatly simplify the process of instrumentation, making SHM much more attainable for many structures. This paper presents a remote camera measurement of the motions of the WWI Memorial Bridge in Portsmouth, NH, a vertical-lift bridge, from

[1]Postdoctoral Associate, Dept. of Civil and Environmental Engineering, Massachusetts Institute of Technology, 77 Massachusetts Ave., Cambridge, MA 02139. E-mail: ju21743@mit.edu

[2]Graduate Student, Dept. of Civil and Environmental Engineering, Univ. of New Hampshire, Durham, NH 03824. E-mail: tmz38@wildcats.unh.edu

[3]Postdoctoral Associate, Dept. of Civil and Environmental Engineering, Massachusetts Institute of Technology, 77 Massachusetts Ave., Cambridge, MA 02139. E-mail: haosun@mit.edu

[4]Chair and Associate Professor, Dept. of Civil and Environmental Engineering, Univ. of New Hampshire, Durham, NH 03824. E-mail: erin.bell@unh.edu

[5]Professor, Dept. of Civil and Environmental Engineering, Massachusetts Institute of Technology, 77 Massachusetts Ave., Cambridge, MA 02139 (corresponding author). E-mail: obuyuk@mit.edu

a distance of over 80 meters. Vibration frequencies and mode shapes of the bridge are identified by measuring the displacements due to the lift span impact. Displacement of the bridge due to in-service traffic is also measured. Measured signals are compared to accelerometers and strain gauges installed on the bridge and identified characteristics of the bridge are compared to a finite element model for verification. Results show the potential of applying video cameras to measure and visualize vibrations of structures in SHM.

Keywords: Video camera, computer vision, vibration analysis, motion magnification, bridge monitoring

INTRODUCTION

An objective basis for asset management is needed as the Moving Ahead for Progress in the 21st Century Act (MAP21) comes into effect (FHWA, USDOT 2012). Visual inspection supports decision making related to infrastructure management but is inherently subjective (Phares et al. 2004). Sensors are increasingly useful for characterizing the conditions of bridges – to augment the data collected through visual inspection – as computational methods and instrumentation have improved over time. By instrumenting bridges with contact sensors such as accelerometers and strain gauges, researchers have been able to evaluate the performance and condition of bridges, and also carry out load ratings important for safety (Lynch et al. 2006; Sanayei et al. 2011; Bell et al. 2013).

Non-contact measurements are particularly desirable as sensors do not need to be physically placed on the bridge, which can often be quite inconvenient or aesthetically unpleasing. One example of a non-contact measurement is the use of interferometric radar (Pieraccini et al. 2006), and another is the use of a laser scanner to measure displacements during bridge load testing (Fuchs et al. 2004).

Videos cameras as measurement tools

Video cameras can be used to collect information remotely from structures as they are capable of recording massive amounts of data in the form of a series of images over time. They have also become increasingly less expensive as technology improves and higher frame rates and resolutions are available to normal consumers. Video cameras have been previously used to measure the motions of bridges using a variety of different image processing techniques (Lee and Shinozuka 2006; Caetano

Chen, August 12, 2017

₄₀ et al. 2011; Kim and Kim 2013; Fukuda et al. 2013; Feng et al. 2015b).

₄₁ A new technique based on phase-based motion magnification is particularly useful for both
₄₂ qualitatively visualizing imperceptible motions in a video, and quantitatively measuring vibrations
₄₃ and displacements (Wadhwa et al. 2013; Wadhwa et al. 2014). This technique can measure the
₄₄ resonant frequencies and mode shapes of structures in a laboratory (Chen et al. 2015; Yang et al.
₄₅ 2017), and at long distances (Chen et al. 2016). The measurement of displacement is additionally
₄₆ important as it is generally difficult for real-world structures and useful for quantifying the full state
₄₇ of motion of a structure. The specific advantage of this technique based on phase-based motion
₄₈ magnification is that displacements can be processed more quickly, smaller motions can be handled,
₄₉ and the visualization of imperceptible motions aids the experimenter in examining the operational
₅₀ mode shapes of a structure.

₅₁ In this paper a case study is presented that uses a camera as a vibration and deflection measure-
₅₂ ment tool for a bridge response with a recently developed video processing technique (Chen et al.
₅₃ 2016). A set of long distance camera measurements of bridge structural response is compared to
₅₄ traditional sensors including research-grade accelerometers and strain gauges. A multi-rate Kalman
₅₅ filter data fusion technique based on Smyth and Wu (2007) is employed to combine the camera and
₅₆ accelerometer measurements to provide more accurate information for structural health monitor-
₅₇ ing purposes. The measurement results are compared to a finite element model of the bridge for
₅₈ validation with respect to the expected structural response. This data is used as a basis for traffic
₅₉ load estimation on the bridge using information from both the displacement measurement and finite
₆₀ element model. Alternative bridge structural health monitoring uses for this collected information
₆₁ are also presented.

₆₂ The main objective of this paper is the end to end study of a large-scale civil structural system
₆₃ with correlation to a finite element model validating the video camera measurement as used for
₆₄ civil infrastructure. Additionally, another contribution is practical suggestions for ways that the
₆₅ method can be implemented for the vibrational characterization and structural health monitoring
₆₆ of civil infrastructure and implications for future use and implementation as to the limitations of
₆₇ the technique.

₆₈ The paper is organized as follows. After the introduction, the theory of video measurement

Chen, August 12, 2017

₆₉ and the processing methodology is discussed. Then, the bridge measurement as a case study is

₇₀ introduced along with the experimental setup. The results of the camera measurement, the data

₇₁ fusion technique, and finite element modeling of the bridge as well as a comparison between the

₇₂ model and camera measurements are presented. A discussion of all the results as well as some

₇₃ practical lessons learned and limitations for outdoor and long-range implementation of the camera

₇₄ methodology are given for future studies. Finally, conclusions are given as well as some proposed

₇₅ future work for video camera measurement of civil infrastructure.

VIDEO DISPLACEMENT MEASUREMENT METHODOLOGY

₇₇ The videos are processed into measured displacements by using a technique inspired by motion

₇₈ magnification (Wadhwa et al. 2013; Wadhwa et al. 2014), using phase-based optical flow (Fleet and

₇₉ Jepson 1990; Gautama and Van Hulle 2002). This technique is detailed in Chen et al. (2015), and

₈₀ summarized here. Each frame of the video is transformed using a local quadrature spatial filter

₈₁ pair, into a spatial phase and amplitude representation of the image. This representation is similar

₈₂ to a local Fourier transform where the amplitude represents the strength of the filter around that

₈₃ pixel and the phase represents the location. Fleet and Jepson (1990) and Gautama and Van Hulle

₈₄ (2002) found that changes in the local phase contours in time are representative of motion, and can

₈₅ be used to determine the motion of objects in the video. Thus, the local phases for the same pixel

₈₆ patches in sequential frames are put together to obtain time series signals that can be translated

₈₇ into displacements of an object at a single point in the frame. By keeping the motions small, within

₈₈ the spatial support of the filter, or within a 2π phase shift, by examining the motion at a single

₈₉ pixel, the true motion is obtained. If motions are too large, features would need to be tracked to

₉₀ determine the true displacement of objects.

₉₁ This shift of representation into local phase space allows for subpixel motions as instead of

₉₂ working on shifts in intensity which can be noisy as cameras have noise in the intensity of pixels,

₉₃ changes in the phase are more robust to that noise and thus smaller displacements can be handled.

₉₄ Within this processing scheme, a motion magnified visualization where small imperceptible motions

₉₅ can be easily seen can be generated (Wadhwa et al. 2013). If the motions are magnified in a tight

₉₆ frequency band matching that of an operational resonant frequency of a structure, the resulting

visualization is of the operational mode shape of the structure at that frequency.

To translate the motion in terms of pixels to physical displacements , the length of a known object in the video relative to it's pixel length is used as a calibration factor, which may depend on the depth of the object and location in the video frame. To obtain a high fidelity displacement signal of a specific location on the structure, the video is cropped in a small region around that location and then processed and averaged together to provide a single displacement signal as the spatial averaging reduces noise from point measurements.

Assumptions

Several assumptions are made to accomplish the video processing to provide measured displacements. The motions must remain relatively small, on the order of a couple of pixels. Lighting conditions need to stay constant as changes in lighting can manifest as apparent motion. The camera itself must remain stationary, as any motion measured is relative motion between the camera and the bridge. These assumptions and limitations are further discussed in the discussion section later in the paper.

EXPERIMENTAL SETUP

This section describes the experimental setup and the rationale for choosing the WWI Memorial Bridge for the study.

WWI Memorial Bridge as a case study

The WWI Memorial Bridge spans the Piscataqua River from Portsmouth, New Hampshire to Badger's Island in Kittery, Maine with a total length 366.1 m (1201 ft). It is a vertical-lift truss bridge with a clearance of 39.6 m (130 ft). The bridge was reconstructed in 2013. Built in 1923, the original vertical-lift Memorial Bridge had to be permanently closed in 2011 for safety and structural concerns. Pictures of the bridge are shown in Figure 1, specifically showing the central lift span.

The lift motions provide consistent excitations that vibrate the bridge, which simplifies the task of SHM. The repeated excitations mitigate some of the challenges associated with excitation variability, and significantly excite the bridge so that it can be measured without waiting for environmental or other external conditions to induce sufficient motion in the bridge. This bridge was chosen to be measured precisely because of these lift motions providing consistent excitations

along with the relatively consistent normal traffic patterns that go across the bridge. Additionally, there was an opportunity to measure the bridge concurrently with both contact sensors and a video camera as the proper permissions were obtained from the overseeing authorities. Vibrations due to the lift span impact excitation and normal deflections due to in-service traffic are measured with the camera system from over 80 meters away. The bridge is also of particular interest because of a new design for the joints in contrast with a typical truss system where the bolted connections are moved onto the diagonals as splices and the joint is integral as a part of the top or bottom chord.

(a)

(b)

(c)

FIG. 1. Pictures of the WWI Memorial Bridge in Portsmouth, NH with (a) center span in a lowered state, (b) center span in a lifted state, and (c) special connection on the bridge with a monolithic joint

Chen, August 12, 2017

Experimental Configuration

A measurement was conducted with the goal of demonstrating that a video camera could measure the vibration characteristics of the bridge and be used in support of a wider SHM system for decision making about the serviceability and maintenance schedule for the bridge. A camera was set up approximately 80 meters (260 feet) away in a nearby park to take video of the NH side fixed span of the bridge. A satellite view of the bridge and measurement location is shown in Figure 2(a). A picture showing the measurement setup and the bridge in the same view is shown in Figure 2(b).

(a)   (b)
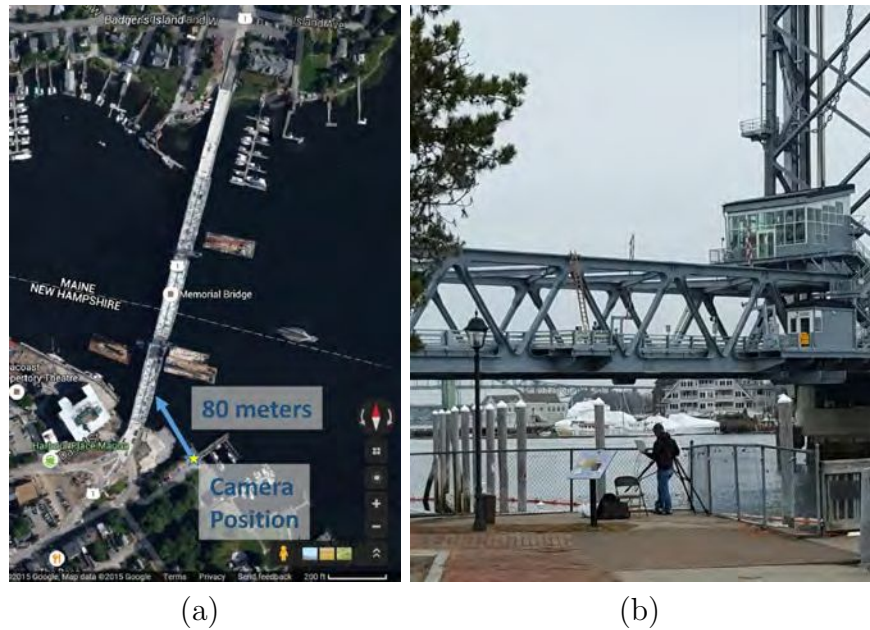
FIG. 2. (a) Satellite view of the camera measurement location relative to the NH span of the bridge and (b) picture of both the camera measurement setup and view of the NH span of the bridge

The camera measurement system consisted of a Point Grey camera, a heavy tripod, a MEMS accelerometer system to measure the camera motions, and a laptop to collect the data. The whole system, seen in Figure 3, is portable and can be run from a set of 12V batteries and an AC inverter for portability.

The measurement was made on December 14, 2015, with an ambient temperature of 48°F and a light drizzle. A picture of the view from the camera location is shown in Figure 4(a), and the camera is covered with a plastic bag to protect it from the precipitation. During this data collection, two accelerometers and two strain gauges were temporarily placed on the bridge to concurrently

FIG. 3. Picture of the camera measurement setup

measure the bridge's vibrations to compare the remote video camera measurement and contact accelerometers and strain gauge sensors. These sensors were sampled at 200 Hz. Figure 4(b) shows the locations of the two accelerometers, A2192 and A2193, and the two strain gauges, B4821 and B4824, on a screenshot directly from the recorded video. The video was recorded with a resolution of 800×600 pixels with a frame rate of 30 frames per second. Time synchronization was accomplished by using a GPS application on cell phones carried by the field engineers at both locations to relate the system times between the camera measurement system laptop and the accelerometer data acquisition laptop. These offsets were then used as a starting point when plotting the two time series to align them in time. Small adjustments were then made by hand, referencing off of the time that the lift impact appears in the time signals, to align the two time series more precisely.

FIG. 4. (a) Picture of the view from the camera with (b) screenshot from the recorded video with comments as to the locations of the accelerometers and strain gauges on the bridge. For A2192 the camera region of interest is centered on the accelerometer location as annotated with size 218 × 92 pixels, while for A2193, the region of interest is directly below the A2193 sensor as annotated with size 300 × 76 pixels.

CAMERA MEASUREMENT

The bridge was excited through two different manners, one was the impact of the lift span of the bridge after a lift, and the other was normal traffic passing over the bridge. Two measurement sets were made during these excitations of the bridge and are presented below.

Lift impact response

A lift was conducted by the bridge operators at approximately 10:30am on December 14, 2015. Figure 5 shows the resulting vertical direction measurements from the accelerometers A2192 and A2193 as compared with the video measurement in a region of interest cropped around the location of the sensor. For A2192 the region of interest is centered on the accelerometer location as annotated in Figure 4(b) with size 218 × 92 pixels, while for A2193, the region of interest is directly below the A2193 sensor as annotated with size 300 × 76 pixels. In Figure 5 the accelerometer measurement is double integrated to produce displacement. In these plots in the time domain in Figures 5 (b) and (d) the for the camera a high pass filter at 0.5 Hz is applied to remove DC and very low frequency noise, while a 10 Hz low pass filter is applied for better plot visibility. For the accelerometer data that is double integrated, after each integration a high pass filter with a cut off frequency of 0.5 Hz is applied to remove low frequency contamination.

Chen, August 12, 2017

For the A2192 accelerometer measurement location, the dimension of the web of the top chord of the bridge [0.61 meters (24 inches) tall] corresponding to 30 pixels in the frame of the video is the basis for conversion of the measured pixel displacements to units of inches. For the comparison with the A2193 accelerometer shown in Figure 5 (c) and (d), the scaling factor is 0.91 meters (36 inches) to 44 pixels. These values are slightly different due to slightly different distances of these locations on the bridge from the camera. Other locations on the bridge at different depths will have different scaling factors and they will need to be determined manually. This calibration is important if physical displacements need to be obtained for the full frame of the video, however it can be tedious for complex structures. A possible way to obtain these calibration factors is given in the future work section in the conclusion using a stereo camera setup. Given that the camera is looking at a slight upwards angle, there is also a small distortion and projection of the true vertical motion on to the vertical image plane of the camera, however given the distance from the camera to the point measured and vertical height of the bridge to calculate this angle, the error is only 1 to 2 percent and neglected in this analysis. Possible solutions to these issues will be given in the conclusion and future work sub section.

In both these comparisons, the resonant frequencies present in the frequency spectra, 1.267 Hz, 1.68 Hz, and 2.52 Hz align for both the accelerometer and the camera. The time series measurements also compare favorably. This measurement shows that the camera measures the same information as an accelerometer from a distance of 80 meters (260 feet).

A full frame video of 1000 frames around the lift span impact was processed. Even though the motion of interest is in the vertical direction and not the horizontal direction, both directions are processed to show the capabilities of the technique to extract general displacements in a perpendicular basis of directions. The downsampled video frame and pixel masks are shown in Figure 6, the extracted average displacement signals shown in Figure 7, and the resulting modeshape phase images for three resonant modes at 1.26 Hz, 1.71 Hz, and 2.52 Hz, are shown in Figure 8.

Chen, August 12, 2017
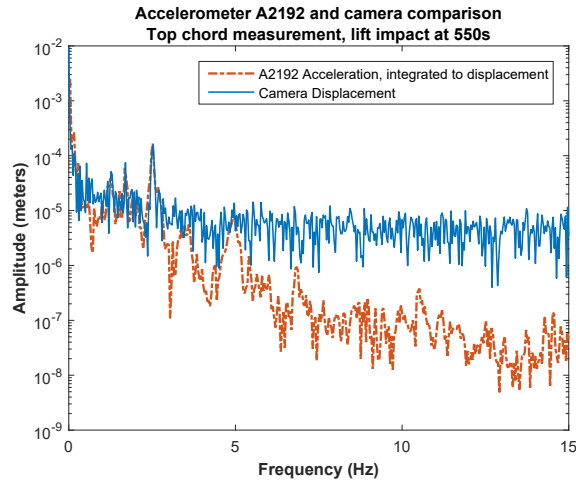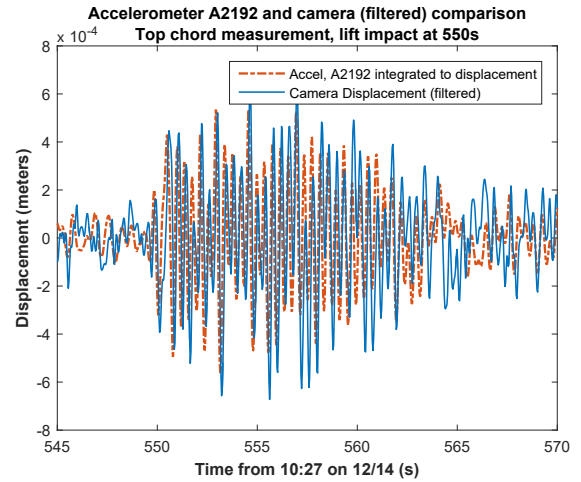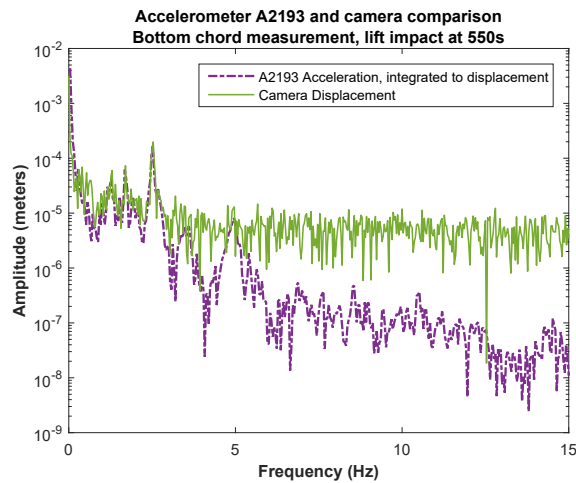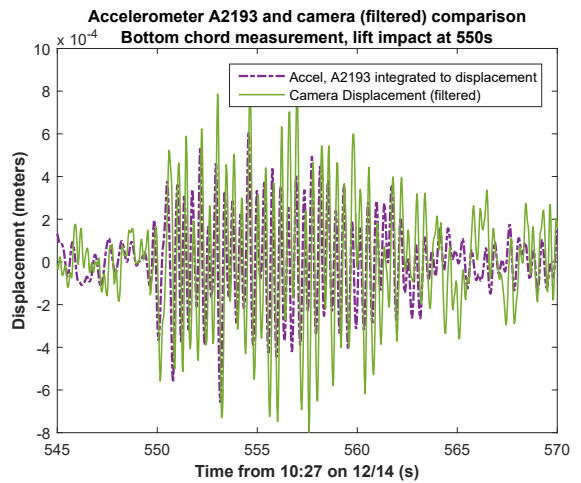
FIG. 5. Comparison of measurements from the camera and accelerometer (double integrated to displacement) for the **A2192** accelerometer in the (a) time domain and (b) frequency domain, and for the **A2193** accelerometer in the (c) time domain and (d) frequency domain. Note that the accelerometer time series ~~in (a) and (c),~~ have a high pass filter with a cut off frequency of 0.5 Hz applied after each integration.

(a)   (b)
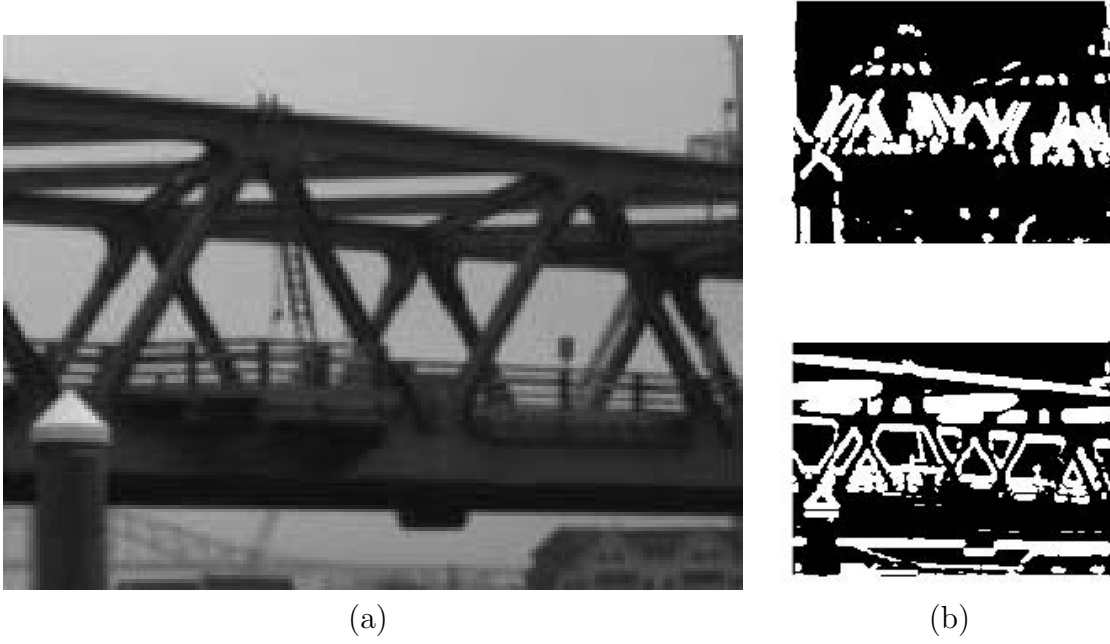
FIG. 6. Processing of the full frame video including (a) Downsampled frame (200 × 150 pixels) and (b) top: horizontal direction and bottom: vertical direction automatically generated image masks for pixels with valid displacements where white pixels are pixels with sufficient local contrast from which reliable displacements can be extracted, and black pixels have insufficient local contrast and no displacements are extracted

(a)   (b)
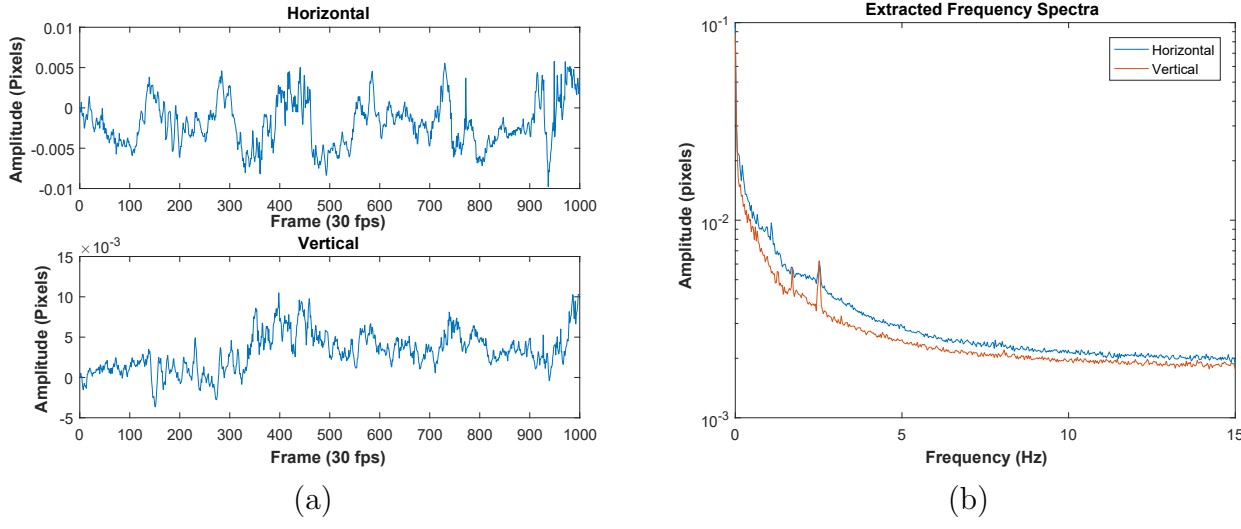
FIG. 7. Average displacement signals for the full frame video for horizontal and vertical directions in the (a) time domain and (b) frequency domain

Chen, August 12, 2017
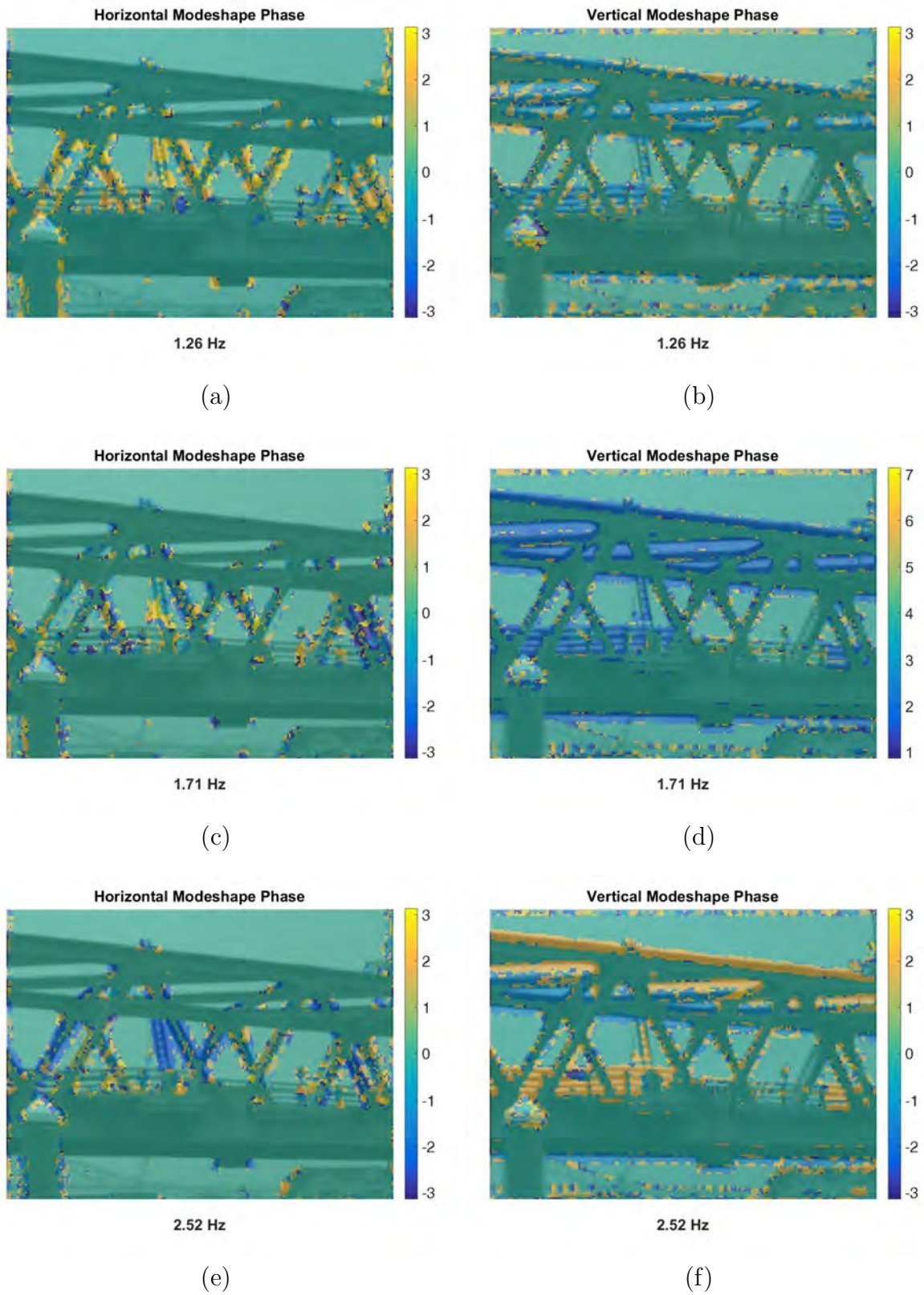
FIG. 8. Modeshape phase images in the horizontal and vertical directions for (a-b) 1.26 Hz, (c-d) 1.71 Hz, (e-f) 2.52 Hz

Chen, August 12, 2017

Traffic induced loading response

Before the lift at 10:30 am, there was normal traffic transiting across the bridge. A video was recorded starting at approximately 10:21:03 am, which begins with a concrete mixer truck at midspan going northbound. Later in the video other cars and smaller pick-up trucks also cross the bridge. Since this was normal traffic operations and not a controlled load test, the true loads on the bridge are not known. To measure the displacement of the bridge, a region of interest is made on the bottom chord at the midspan of the bridge, and another region of interest is selected below that of a stationary object in the background as a reference for the purpose of removing camera motion. A screenshot from the start of the video with the regions of interest outlined is shown in Figure 9.

FIG. 9. Screenshot from the start of the 10:21:03 am video showing a concrete mixer truck and regions of interest boxed on the bottom chord and an object in the background for reference

Vertical displacements were extracted from these regions of interest, from the bottom chord and the stationary reference are shown in Figure 10(a). To compensate for motion of the camera, the stationary reference signal was subtracted from the signal from the bottom chord, both in units of pixels to obtain the motion compensated signal. Even though the two objects are at different depths in the scene, under an assumption of small rotations of the camera, the apparent motions of both objects due to camera motion will be equivalent in units of pixels in the image plane.

We can offset the motion compensated by 0.208 pixels to give the displacement in pixels of the

Chen, August 12, 2017
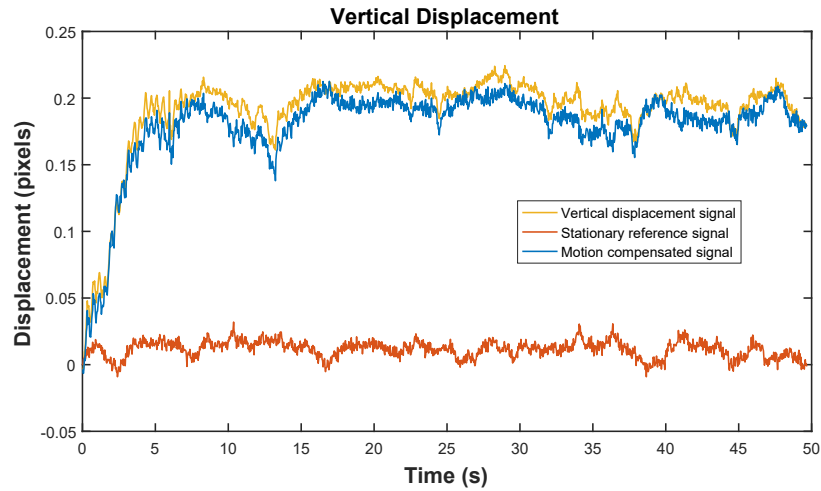
(a)
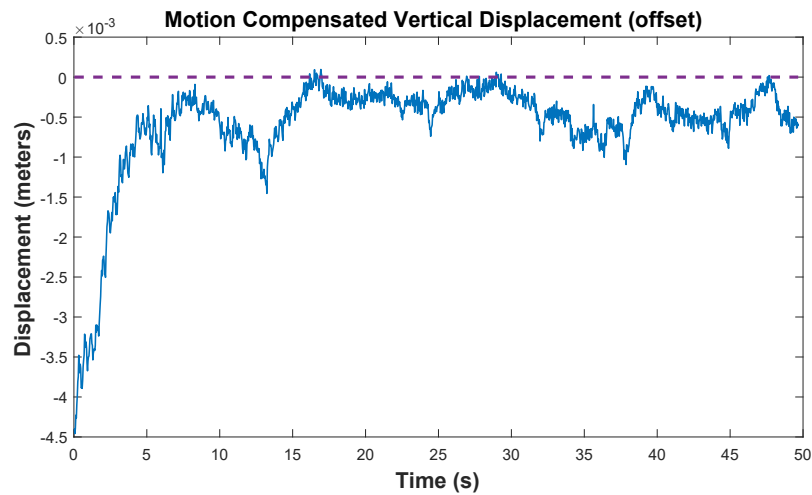
(b)

FIG. 10. Vertical displacements extracted from the video measuring traffic induced loading with (a) measured signals including displacement from the bottom chord, displacement from a background stationary object, and the motion compensated signal from the bottom chord, and (b) motion compensated vertical displacement of the bottom chord in inches, approximately offset to represent the displacement from an unloaded state, a dashed line

bridge from an estimated unloaded state. This amount is determined by approximately lining up the highest vertical displacements seen with a zero line. To translate from units of pixels to inches displacement at the bridge, we use the fact that the web of the bottom chord is 44 pixels in the video and 0.91 meters (36 inches) tall. The resulting measured vertical displacement of the bottom chord of the bridge is shown in Figure 10(b).

A comparison was made to the measurement from a strain gauge placed on the bridge, shown

Chen, August 12, 2017

²²¹ as B4821 in Figure 4(b) measuring longitudinal of the top flange of the top chord. To compare

²²² this measurement with the camera measured displacement, they are aligned in time and the strain

²²³ measurement amplitudes are scaled by a factor of $\frac{1}{6000}$ to visually match the camera measurement.

²²⁴ The two measurements can be compared because the bridge can be reasonably approximated by

²²⁵ an Euler-Bernoulli beam, in which the axial strain will be proportional to the beam curvature or

²²⁶ second derivative of deflection with respect to location. An assumption is made for the response of

²²⁷ the bridge due to traffic loading that it is slow enough be considered quasi-static as the deflection

²²⁸ of an Euler-Bernoulli beam is not necessarily proportional to the second derivative of the deflection

²²⁹ (i.e. strain) with respect to location for dynamic responses. The results are shown in Figure 11

²³⁰ showing good correlation between the behavior of the B4821 strain measurement on the top chord

²³¹ and the camera measured vertical displacement of the bottom chord.
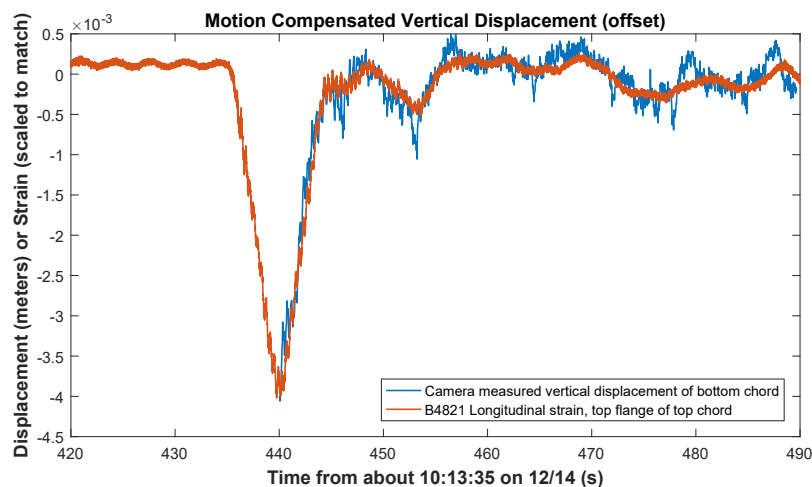
FIG. 11. Comparison of displacement measurement (meters) with strain gauge measurements with magnitudes scaled to match (microstrain/6000)

SENSOR FUSION

²³³ As measurements in the real world are inherently noisy, and double integration of accelerometer

²³⁴ measurements can be difficult, displacement measurements derived from a camera and accelerome-

²³⁵ ters may not be perfectly matched (Worden 1990). A sensor fusion methodology can reconcile the

²³⁶ two disparate data sources and may also account for different sampling rates. We can use a multi-

²³⁷ rate Kalman Filter methodology for sensor fusion to obtain a better estimate of the camera motion

Chen, August 12, 2017

from both an image-space measurement of the camera motion and accelerometer measurement on the structure of interest as previously done by Smyth and Wu (2007).

Multi-rate Kalman Filter formulation

A summary of the multi-rate Kalman filter formulation presented in (Smyth and Wu 2007) is given here. The state-space formulation of the camera and accelerometer measurements as a discrete process can be modeled as follows:

$$
\begin{bmatrix} x(k+1) \\ \dot{x}(k+1) \end{bmatrix} = \begin{bmatrix} 1 & t_a \\ 0 & 1 \end{bmatrix} \begin{bmatrix} x(k) \\ \dot{x}(k) \end{bmatrix} + \begin{bmatrix} t_a^2/2 \\ t_a \end{bmatrix} \ddot{x}_m(k) + \begin{bmatrix} t_a^2/2 \\ t_a \end{bmatrix} \eta_a(k) \tag{1}
$$

$$
z(k) = x_m(k) = \begin{bmatrix} 1 & 0 \end{bmatrix} \begin{bmatrix} x(k) \\ \dot{x}(k) \end{bmatrix} + \eta_d(k) \tag{2}
$$

with x representing the system displacement, $\dot{x}$ the velocity, and $\ddot{x}$ the acceleration, t_a the time interval for the accelerometer measurement, k as the time step, x_m and $\ddot{x}_m$ the measured displacement and accelerations, and η_d and η_a the associated measurement noise for the displacement and acceleration. These equations can be written compactly (changing $\ddot{x}_m$ to u(k) for the canonical notation) as:

$$
\mathbf{x}(k+1) = \mathbf{A}\mathbf{x}(k) + \mathbf{B}u(k) + w(k) \tag{3}
$$

$$
z(k) = \mathbf{H}\mathbf{x}(k) + v(k). \tag{4}
$$

where $\mathbf{A}$ and $\mathbf{B}$ are as described in equation (1) and $\mathbf{H}$ is as described in equation (2). $\mathbf{x}(k)$ represents the system state of displacement and velocity, $u(k)$ is the acceleration, and $w(k)$ represents measurement noise term $\eta_a(k)$ for the acceleration. $v(k)$ represents the measurement noise term for the displacement $\eta_d(k)$. The covariance matrices of the noise sequences are:

$$
\mathbf{Q} = \begin{bmatrix} qt_a^3/3 & qt_a^2/2 \\ qt_a^2/2 & qt_a \end{bmatrix} \tag{5}
$$

$$
\mathbf{R} = \frac{r}{t_a} \tag{6}
$$

where q is a covariance for the acceleration measurement noise, and r is a covariance for the displacement measurement noise.

The Kalman filter is an algorithm that produces estimates of unknown variables of a system from a series of measurements, given some input characteristics about the process variance and the measurement noise. From the state space formulation of the measurement, the Kalman filter algorithm is as follows with the time update step:

$$\hat{\mathbf{x}}(k+1|k) = \mathbf{A}\hat{\mathbf{x}}(k|k) + \mathbf{B}u(k) \tag{7}$$

$$\mathbf{P}(k+1|k) = \mathbf{A}\mathbf{P}(k|k)\mathbf{A}^T + \mathbf{Q} \tag{8}$$

and the measurement update step which includes the Kalman gain $\mathbf{K}$ and the estimate covariance $\mathbf{P}$:

$$\hat{\mathbf{x}}(k+1|k+1) = \hat{\mathbf{x}}(k+1|k) + \mathbf{K}(k+1)[z(k+1) - \mathbf{H}\hat{\mathbf{x}}(k+1|k)] \tag{9}$$

$$\mathbf{P}(k+1|k+1) = [\mathbf{I} - \mathbf{K}(k+1)\mathbf{H}]\mathbf{P}(k+1|k) \tag{10}$$

and the Kalman gain $\mathbf{K}(k+1)$ is given by

$$\mathbf{K}(k+1) = \mathbf{P}(k+1|k)\mathbf{H}^T[\mathbf{H}\mathbf{P}(k+1|k)\mathbf{H}^T + \mathbf{R}]^{-1} \tag{11}$$

To fuse displacement and acceleration measurements, made at different sampling rates, a multi-rate process can be used (Smyth and Wu 2007). We assume that the displacement sampling interval t_d is an integer multiple M of the acceleration sampling interval t_a, where $t_d/t_a = M$. Only the time update is performed during the accelerometer measurement time steps, and then every displacement measurement interval t_d the full Kalman measurement update is performed.

Results

The camera-based displacement measurements and acceleration measurements from the A2192 accelerometer are used as a proof of concept for fusing the two measurement sources without any explicit integration. The measurement noise values for the covariance matrices $\mathbf{Q}$ and $\mathbf{R}$ are derived directly from the measurements during a section without any motion. Figure 12 shows the results

of the Kalman filter sensor fusion algorithm, which produces a self consistent set displacement, velocity, and acceleration signals that take into account the noisy measurement from both the camera and accelerometer. The acceleration derived from the Kalman filter result for the velocity is much closer to the accelerometer measurement and much less noisy than the double derivative of the camera displacement measurement. With some additional statistical methods, this could be used to improve the estimates for velocity and acceleration measurements derived from the camera displacement measurement at locations on the structure not near an accelerometer.
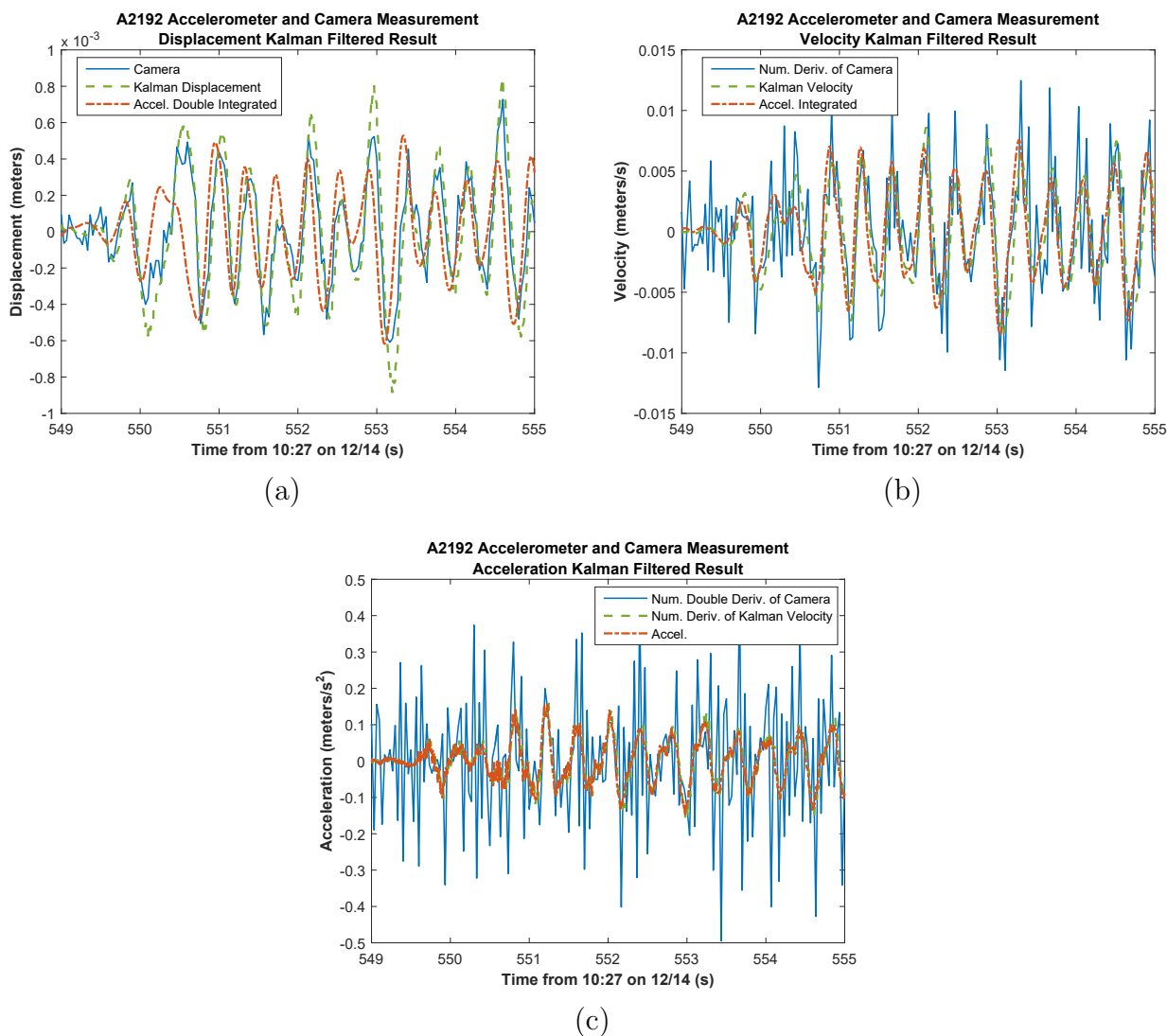
FIG. 12. Kalman filter sensor fusion results with camera and A2192 accelerometer measurement for (a) displacement, (b) velocity, and (c) acceleration

FINITE ELEMENT MODEL

This section details the creation of a ~~finite element~~ model for the Portsmouth bridge for comparison with the resonant frequencies and mode shapes measured by the camera from the bridge. ~~The goal of this section is not to construct a finite element model that matches the measurement results, as that would be relatively meaningless as almost any model could be tuned to precisely match a measurement. Instead, the main purpose was to create a model of the bridge unconnected to any a priori information from the measurement to verify that the dynamics of the bridge reasonably and qualitatively match the behavior as measured.~~

Model Construction

From careful examination of the plans, the central lift span moves on rails on the two fixed spans, and are otherwise not structurally connected. Since the south New Hampshire fixed span is the only one measured by the camera, the model only includes the south fixed truss and lift tower.

The majority of the elements used in the bridge are I beams of various different sections, so for simplicity we choose to model the bridge using beam elements. The only non I beam element is the portal beam at the end of the fixed truss, and this is approximated with a hollo rectangular section beam with the same dimensions. The I beams are made from AASHTO M270 Grade 50 structural steel which is assumed to have a Young's Modulus of 29,700 ksi, a Poisson's ratio of 0.29, and a density of 0.284 lb/in^3.

There is a centering device for the lift span which centers the span as it is lowered and finally seats on to the supports at the end of the lift. If there is slight misalignment, the lift span may end up impacting the support pier as the centering device is engaged and the lift span is lowered into position. This is what may cause the lift impact excitation in the real bridge and is how the excitation was modeled.

Assumptions and Simplifications

The concrete and asphalt deck is modeled as a rectangular cross-section beam, of 11.75" thick and width of 32', with the material properties of concrete, a density of 0.0868 lb/in^3, Young's Modulus of 4000 ksi, and Poisson's ratio of 0.2. This beam approximating the bridge deck is connected to the floor beams that span between the trusses of the lift span. This may result in

Chen, August 12, 2017

³²³ some local modes, however the general bridge behavior should remain well approximated.

³²⁴ The counterweight mass is accounted for by making the girder at the top of the tower heavy

³²⁵ enough to match the weight of the counterweight, as it is fully supported by the east and west

³²⁶ sheave. This effectively applies the mass to those nodes in the model, however it does not account

³²⁷ for the swinging of the counterweight on it's cables, nor the balance chains, which are assumed to

³²⁸ be small effects.

³²⁹ As seen in the pictures in Figure 13, this bridge has connections of a special design where

³³⁰ the joint is an integral element as part of the bottom or top chord, and the typical gusset plates

³³¹ which connect the truss elements are not needed. Connections between elements are instead made as

³³² splices beyond the truss joint. Splice plates connect both the web and the flange parts of the I beams

³³³ on both sides, and thus the connections can transmit moment. To account for this connection, we

³³⁴ use an approximate model where elements in the bridge as assumed to connect at a single point,

³³⁵ rather than modeling the full joint as it would be far too computationally intensive as the joint

³³⁶ would need to be fully modeled using solid elements. We assume a frame behavior at all the joints

³³⁷ in the bridge which transmits moments between the beam elements.

(a)   (b)

FIG. 13. Pictures of the special connections on the bridge with a monolithic joint and the gusset plates moved onto the elements with pictures from the (a) bridge interior showing diagonal supports between the trusses and (b) bridge exterior

³³⁸ The connection between the south tower and the fixed truss span is shown, highlighted in Figure

³³⁹ 14. They are tied together by the gusset plates that connect the twin elements for that triangle of

the truss shared by both the fixed truss and tower. In the model we approximate this with a tie condition between the corresponding nodes in the model so that they are constrained to translate and rotate together.

FIG. 14. Picture of the south tower and fixed truss with the truss-tower connection outlined showing gusset plates tying the two together

There are details of the bridge such as the bridge tender house, stairways, sidewalks, and others that are neglected for modeling simplicity. The main elements of the lift tower, fixed truss span, bridge deck, and counterweight are included in the model.

The boundary conditions for the bridge are pinned at the two nodes for the lift tower and fixed truss side of the bridge, and a roller at the two nodes on the other end, as the bearings in the plans show a fixed and an expansion bearing at these locations respectively. Damping is not included in the model as that would require much more model tuning to get that value correct due to the multiple sources of damping in the actual bridge (e.g. connection, material, support, etc.).

Chen, August 12, 2017

Model Creation

The resulting model was created in Abaqus FEA finite element software, and uses 1790 linear beam elements, with 1637 nodes and a total of 9776 unrestrained degrees of freedom, shown in Figure 15. A high density element mesh was used to ensure that the model would not have any simulator errors, as memory or computational problem was not expected to be an issue with linear beam elements. This model is used as a basis for comparison with the camera measurements by conducting a time history analysis to simulate the impact from the lift span, and an eigenvalue frequency analysis to determine the mode shapes of the resonant frequencies that participate in the response from the time history analysis. This model is derived directly only from the information from the acquired plans and pictures of the bridge provided by the New Hampshire Department of Transportation (NHDOT). The bridge vibration behavior from the camera or accelerometer measurements of the real-world bridge is not used to calibrate the model in any way.
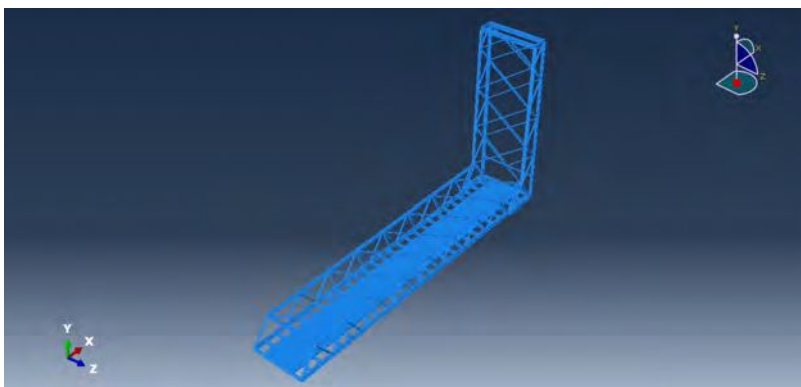
(a)
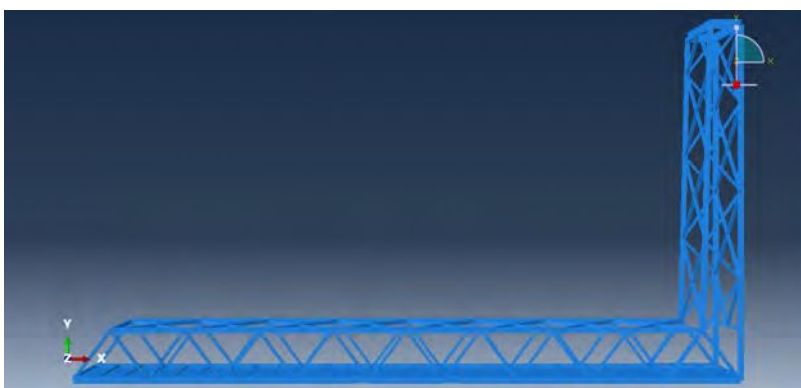
(b)

FIG. 15. Bridge modeled in Abaqus FEA from a (a) front isometric view and (b) side view

Time History Analysis

To simulate the impact of the lift span on the support holding the tower and truss side of the fixed span of the bridge, the boundary condition is displaced vertically downwards by 25.4 mm (1 inch) for 0.1 seconds at the beginning of the simulation.

Rayleigh damping was added to the model with the parameters of $\alpha = 0$ and $\beta = 0.001$ for the steel, and $\alpha = 0$ and $\beta = 0.003$ for the concrete deck. This results in approximately 0.4% damping for the structure at 1 Hz. This was done for a more realistic simulation of the structure's motion, as high frequency local modes would be more quickly damped out and lower frequency modes would remain.

An implicit time history analysis was carried out over 20 seconds with a fixed time step of 0.01 seconds. Since the majority of the response is expected to be under 10 Hz, as has been measured from the bridge, the time step of 0.01 seconds, a factor of 10 shorter than the period of 0.1 seconds for 10 Hz, is sufficient. Figure 16(a) shows the first frame of the time history, showing the displacement of the support at the tower end. Figure 16(b) shows the 59th frame 0.59 seconds into the analysis showing the vibrations having propagated through the bridge and tower. The resulting video of the time history analysis is shown at `https://youtu.be/lqLzNJjR-gM`.

The resulting displacements for the midspan node on the top chord is shown in Figure 17. The dominant response at that node is at 1.6 Hz. The first four modes with significant response are 1.25 Hz, 1.6 Hz, 1.9 Hz, and 2.9 Hz. In order to see the mode shapes corresponding to these frequencies, an eigenvalue frequency analysis is carried out.

Eigenvalue Frequency Analysis

The first 30 modes from the eigenvalue frequency analysis for the undamped bridge model are given in Table 1. The first four modes with significant response in the time history analysis correspond to mode 7 at 1.248 Hz, mode 10 at 1.598 Hz, mode 12 at 1.890 Hz, and mode 20 at 2.892 Hz. The mode shapes for these four modes are shown in Figure 18. Modes 7, 10, and 12 involve some form of tower motion and a first bending mode of the truss fixed span. Mode 20 is a torsional mode of the bridge, where the truss fixed span is rotating and twisting about its longitudinal axis.
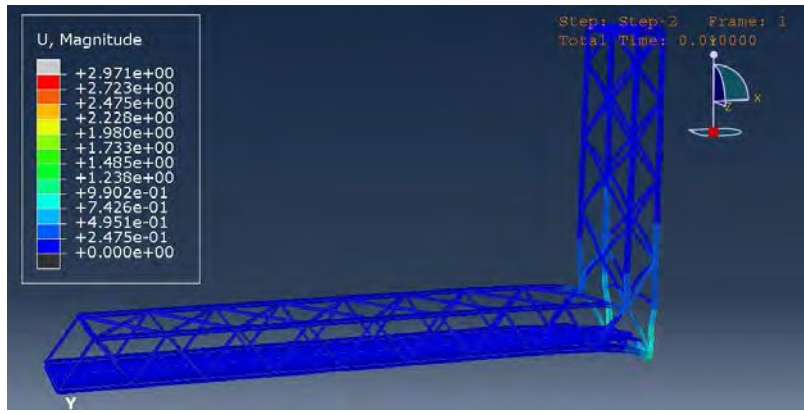
(a)
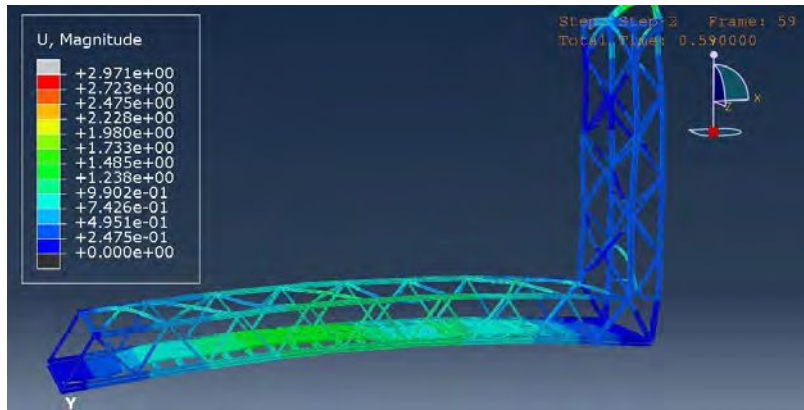
(b)

FIG. 16. Frames from the time history analysis of the bridge showing the displacement magnitude over a deformed model of the bridge with a scale factor of 100 at (a) the first frame showing the impact at the beginning of the time history and (b) the 59th frame or 0.59 seconds into the analysis

TABLE 1. Frequencies of the first 30 modes from the eigenvalue frequency analysis for the bridge model

Mode	Frequency (Hz)	Mode	Frequency (Hz)	Mode	Frequency (Hz)
1	0.327	11	1.704	21	3.111
2	0.377	12	1.890	22	3.558
3	0.533	13	1.949	23	3.738
4	0.745	14	1.983	24	3.756
5	0.880	15	2.147	25	3.925
6	1.094	16	2.188	26	4.031
7	1.248	17	2.292	27	4.140
8	1.416	18	2.380	28	4.257
9	1.524	19	2.833	29	4.413
10	1.598	20	2.892	30	4.781

Chen, August 12, 2017
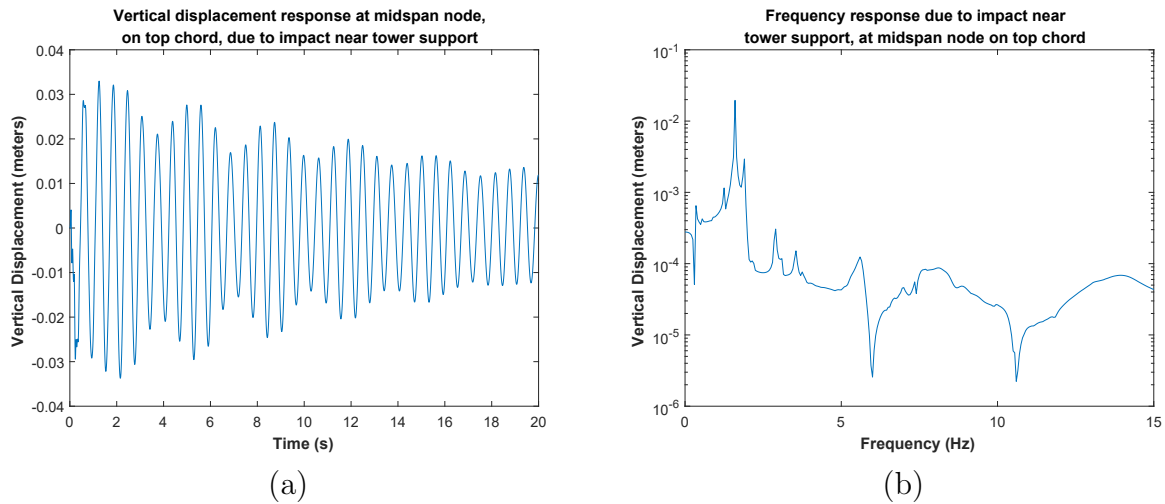
FIG. 17. Vertical displacement of the bridge at the midspan node on the top chord for the time history analysis with damping, (a) time series and (b) frequency spectrum
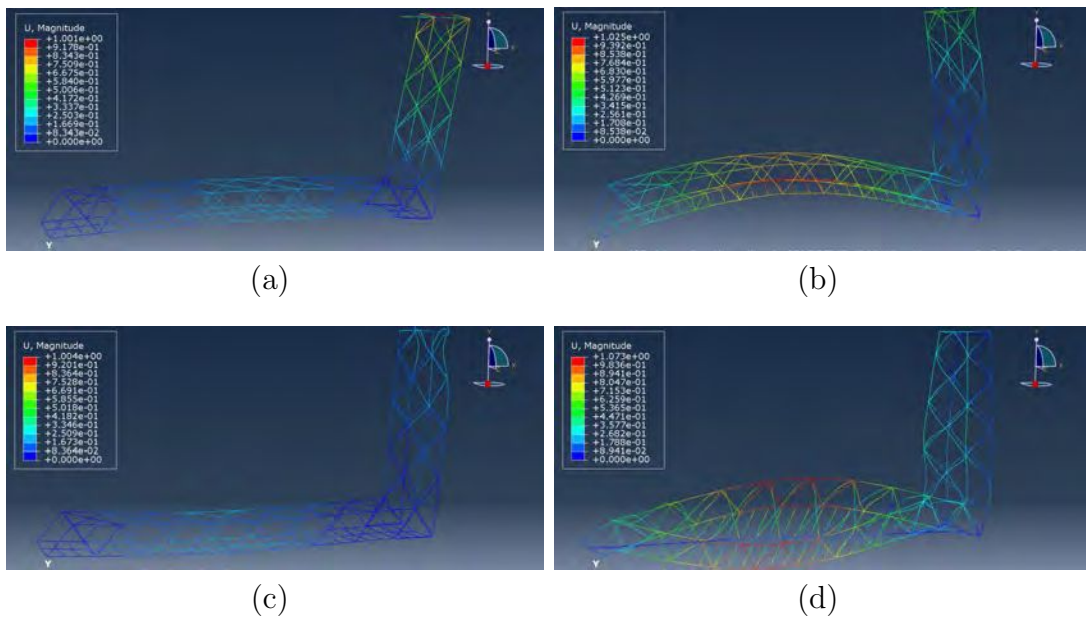
FIG. 18. Mode shapes for the bridge model at the first four frequencies with significant response in the time history analysis, (a) mode 7, 1.2476 Hz, (b) mode 10, 1.5983 Hz, (c) mode 12, 1.8903 Hz, and (d) mode 20, 2.8921 Hz (torsion)

Static Load Analysis

390

391 A static load analysis was also conducted to determine the approximate deflection of the bridge

392 at midspan due to traffic driving across the bridge. Point loads of 1112 N (250 lbf) were applied

393 to four nodes at the center on the northbound side of the fixed truss for a total loading of 4448 N

³⁹⁴ (1000 lbf), as seen in Figure 19. This approximates a 454 kg (1000 lb) load on the northbound lane

³⁹⁵ of the bridge at midspan.
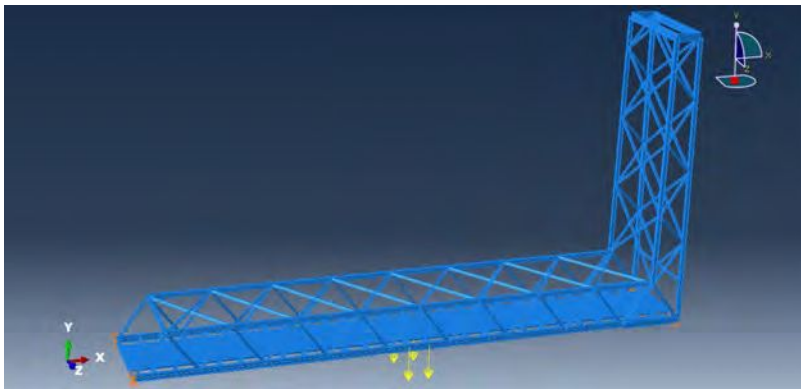
FIG. 19. Load applied at four central nodes on the northbound side, total loading of 4448 N (1000 lbf)

³⁹⁶ The result from the static load analysis is shown in Figure 20, showing the vertical displacements

³⁹⁷ on a deformed model. The average displacement at the two nodes on the centerline of the bridge

³⁹⁸ was -0.136 mm (-0.00535 inches), and the average displacement for the two nodes on the near side of

³⁹⁹ the bridge was -0.129 mm (-0.00506 inches). We can use this information to correlate displacements

⁴⁰⁰ measured in the real world bridge to approximate the imposed loads.
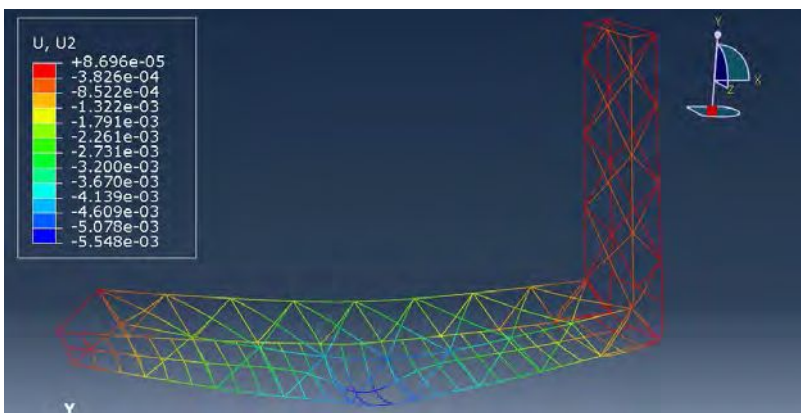
FIG. 20. Static load analysis result showing vertical displacement on the deformed model

⁴⁰¹ **COMPARISON BETWEEN MEASUREMENT AND FINITE ELEMENT MODEL**

Lift Impact Response Comparison

To compare the results from the finite element model and camera measurements of the bridge, we examine the responses to a lift span impact. Figure 21 shows the frequency spectra for the finite element model and both camera measurements. The frequency peaks almost directly compare between the model and the camera measurement, 1.25 Hz and 1.267 Hz, 1.6 Hz and 1.7 Hz, and 2.9 Hz and 2.533 Hz, respectively. Frequency wise, the difference between the frequencies of the torsional modes is the largest between the real bridge and the model, however note that the mode was only constructed from the plans and pictures of the bridge, and has not been massaged to match any of the measurements.
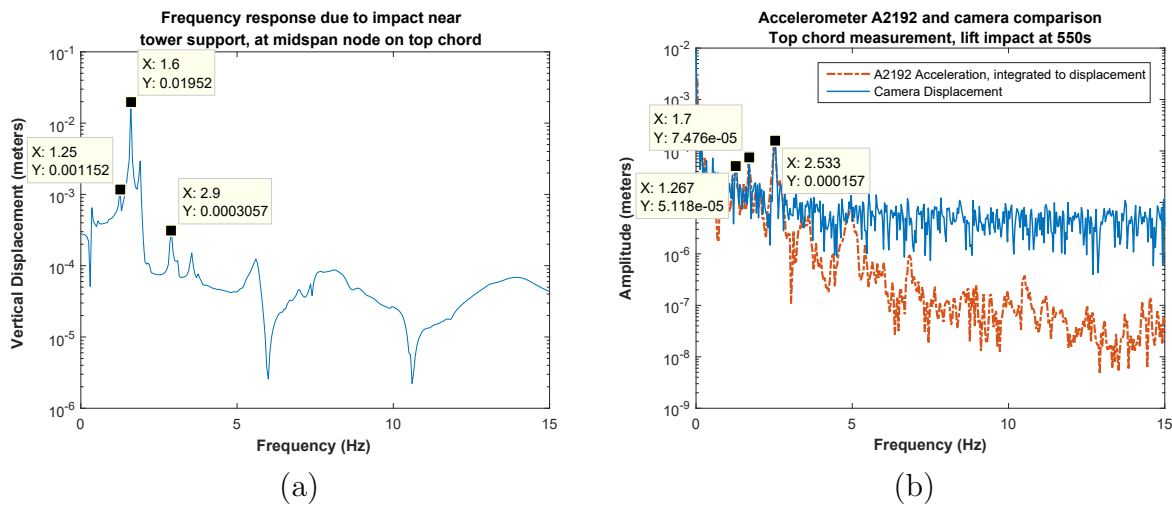
FIG. 21. Comparison of frequency spectra from the (a) finite element model, (b) top node of the Portsmouth bridge, camera measurement

The time domain responses for the model at the midspan node on the top chord can be qualitatively compared to the measurement by the camera at the location of the A2192 accelerometer, in the same location. The two responses are shown side by side in Figure 22. The responses may look dissimilar due to the idealized approximation of the loading from the lift span impact as an impulse and an assumed damping in the model. The peak to peak displacement of approximately 0.03 pixels in the measurement corresponds to approximately 0.635 mm (0.025 inches) of displacement. In the simulation the support is displaced by 25.4 mm (1 inch), and the node moves with an peak to peak displacement of 76.2 mm (3 inches). Since the analysis is completely linear, we can scale

Chen, August 12, 2017

the values down and estimate that an equivalent support displacement of 0.21 mm (0.0083 inches) would cause a peak to peak displacement of 0.635 mm (0.025 inches). This may suggest that the impact of the lift span effectively displaces the support of the bridge by that amount to cause the vibration in the fixed truss.
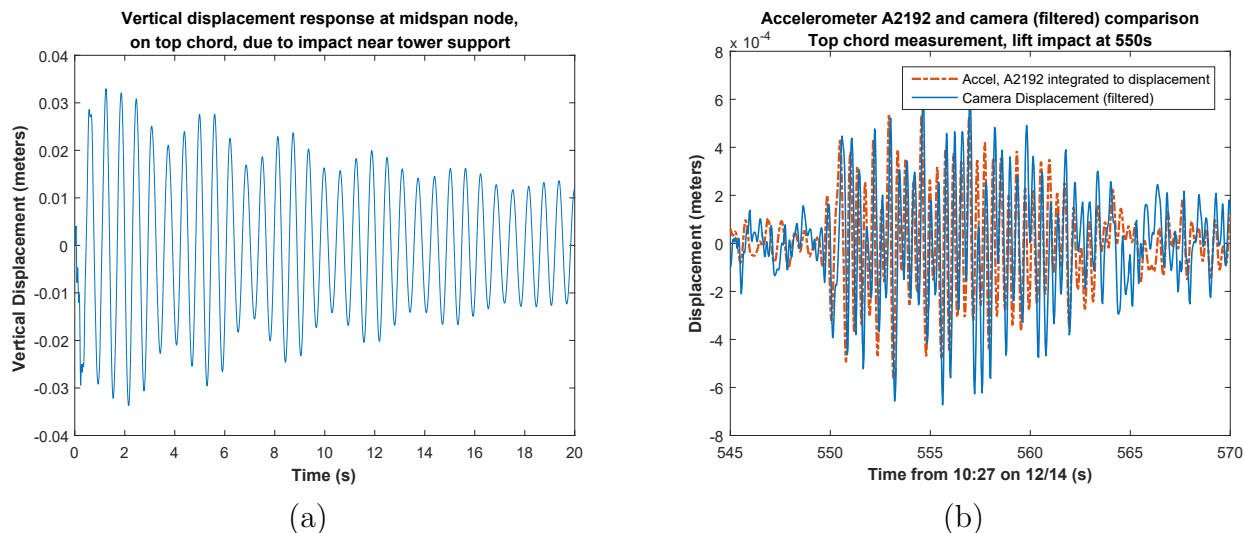
FIG. 22. Comparison of responses due to a lift span impact for the (a) finite element model (b) as measured by both a camera from long-range and an accelerometer on the bridge

Mode Shape Comparison

We can compare representations for the torsional mode shape at 2.89 Hz in the finite element model and 2.52 Hz in the real bridge as shown in Figure 23. The representations look very similar and the animation of the model matches the apparent motion in the motion magnified video of the bridge at the frequency of the torsional mode. The animation of the model at 1.6 Hz where the fixed truss has a vertical bending mode also matches the motion magnified video of the bridge at 1.7 Hz.

Traffic Induced Loading Measurement

In-service traffic loads are important to the operations of a bridge. The measurement of the vertical displacement of the bridge under traffic induced loading can be combined with the static load analysis from the finite element model to estimate the weight of the traffic load on the bridge. The static load analysis tells us that a 4448 N (1000 lbf) at the midspan of the bridge on the
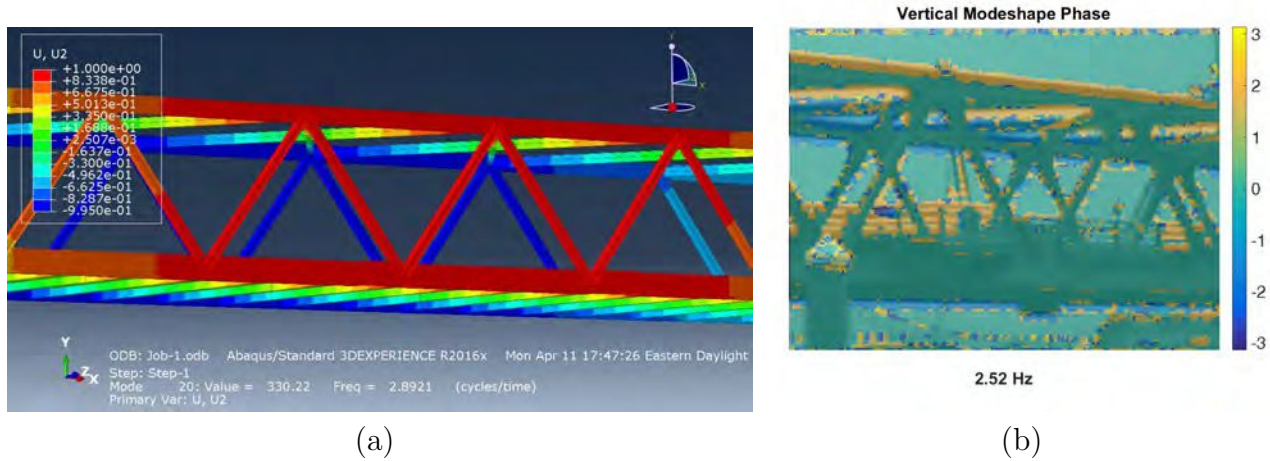
FIG. 23. Comparison of representations of the modeshape for the torsional mode (a) vertical component of the modeshape at 2.89 Hz for mode 20 of the finite element model and (b) image of the vertical direction modeshape phase at 2.52 Hz

northbound side will displace the bridge at the center vertically by approximately 0.127 mm (0.005 inches). Given that for a simple beam with a concentrated load at the center, the maximum displacement at the center will vary directly proportionally with the applied load, we make the assumption that we can estimate the load on the bridge by taking the displacement measured by the camera and scaling that by the 4448 N (1000 lbf) per 0.127 mm (0.005 inches) of displacement. We combine the raw video and the data from the measurement scaled to give an estimated load at the midspan of the bridge to see the loadings of certain vehicles as they drive across the bridge. Figures 24 through 28 show vehicles and estimated loads at different times in the video. The measurement gives plausible loads on the bridge for the weights of the vehicles seen in the video. Since this was not a controlled load test, and the measurement was made during normal traffic operations, it is impossible to know the the actual weights of the vehicles transiting the bridge.

Chen, August 12, 2017
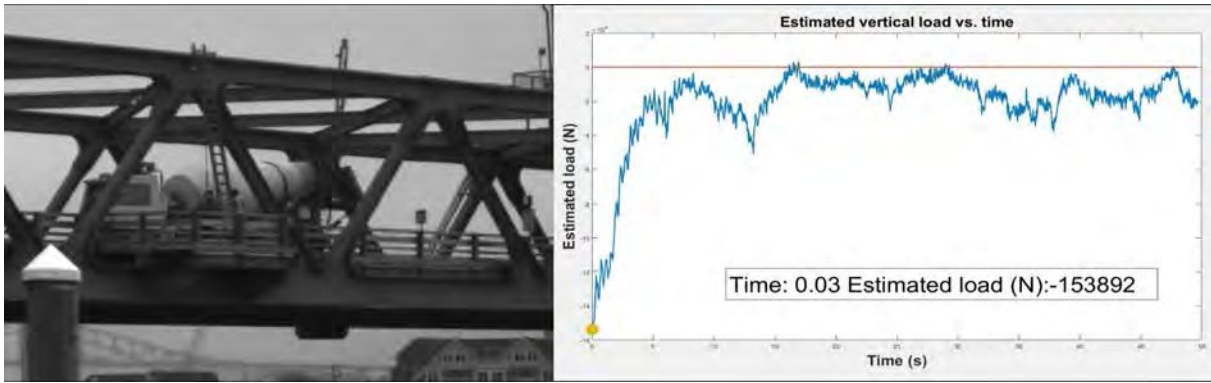
FIG. 24. Concrete truck at 0.03s in the video and estimated load of 153,892 N (34,598 lbf)
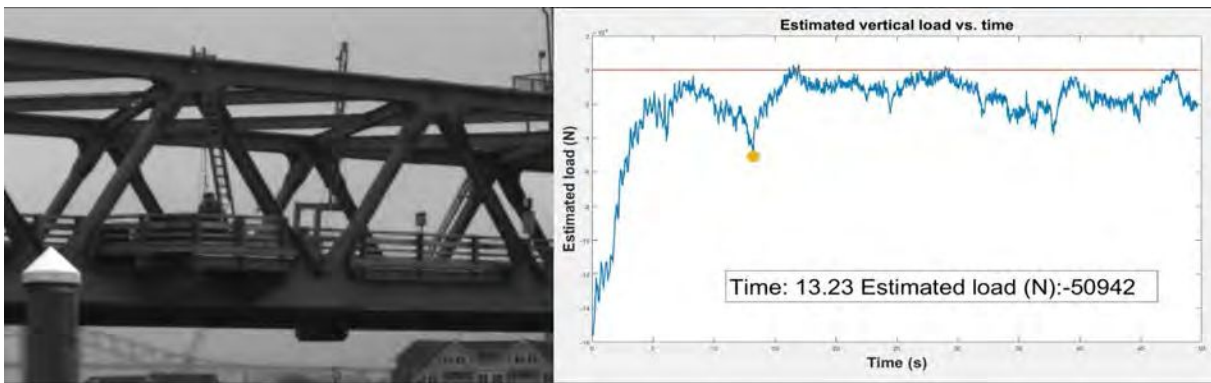
FIG. 25. Heavy work truck at 13.23s in the video and estimated load of 50,942 N (11,453 lbf)
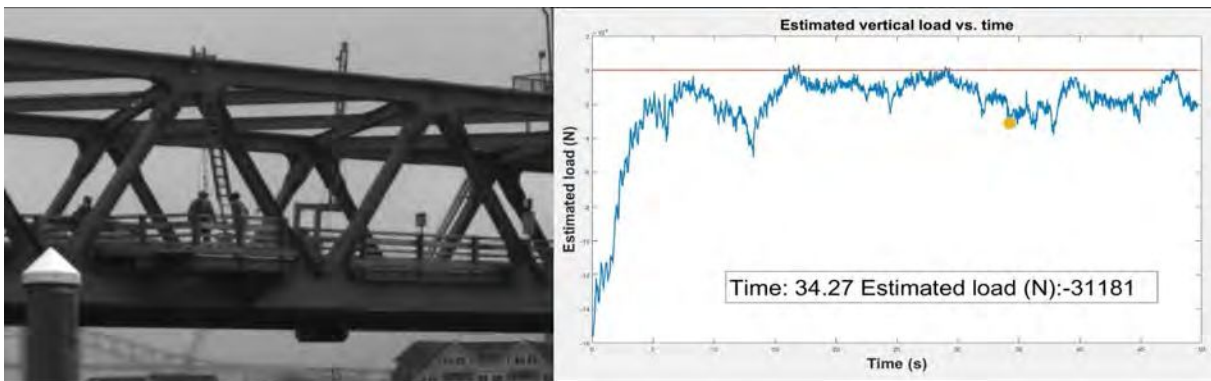
FIG. 26. Crossover SUV at 34.27s in the video and estimated load of 31,181 N (7,010 lbf)
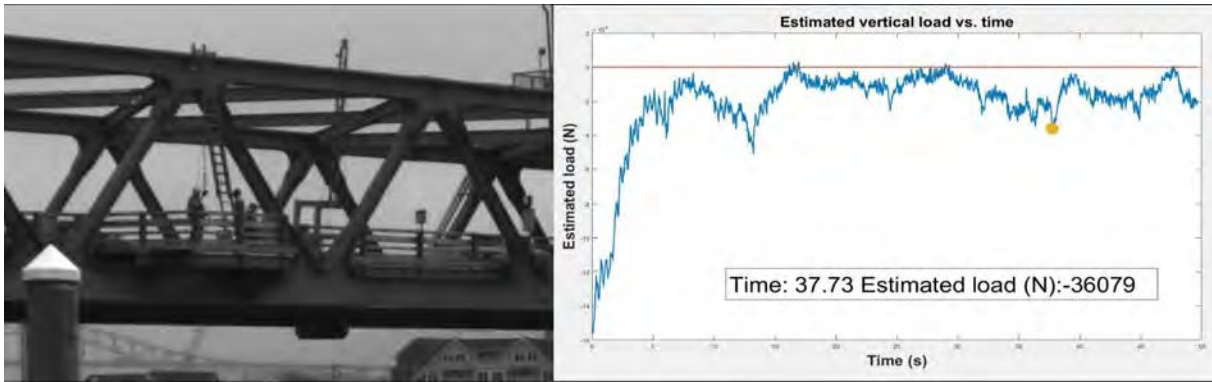
FIG. 27. Sedan and truck nearby at 37.73s in the video and estimated equivalent load of 36,079 N (8,111 lbf)
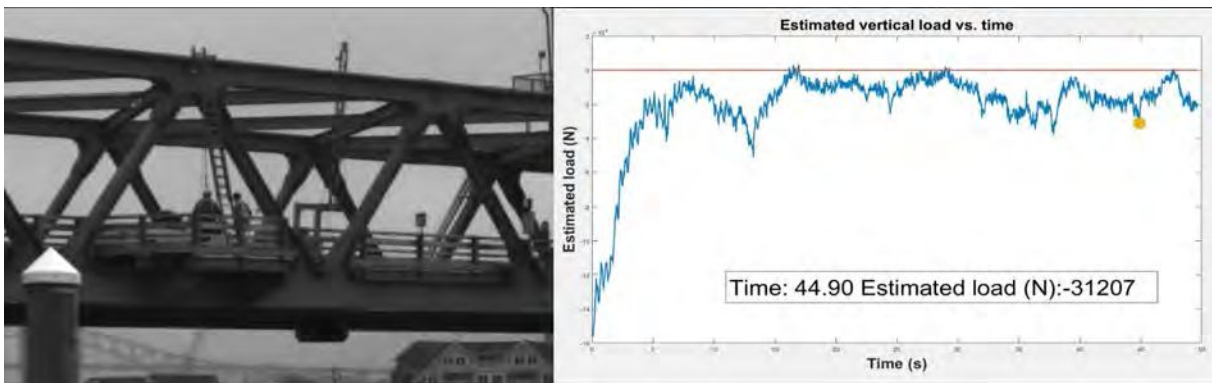
FIG. 28. Pickup truck at 44.90s in the video and estimated load of 31,207 N (7,016 lbf)

Chen, August 12, 2017

DISCUSSION

The camera obtains displacement measurements over many locations over the structure and can build relatively high spatial resolution mode shapes, with good frequency accuracy, however with amplitude values less accurate than traditional accelerometers. The finite element model presented here is likely not sufficiently accurate when compared to the real world structure to be useful for structural health monitoring, however the model could be tuned using the camera measurements. Model updating would ensure that the model matches the current state of the bridge as there may be slight deviations from the plans as built (Mottershead and Friswell 1993; Yuen and Kuok 2011; Sun and Betti 2015; Sun and Büyüköztürk 2016). Even though the bridge is very new and was opened in 2013, one of its piers has already been struck by a boat albeit causing superficial damage to the fender system (Boynton 2014).

Traffic cameras on a bridge could augment a contact sensor and camera measurement system by providing arrival times and approximate sizes of approaching traffic to better identify the traffic loads (Chen et al. 2006). With traffic and other operational and environmental loads identified, the information could be fed into a model to better determine the remaining fatigue life of the bridge, using S-N curves (Zhou 2006). Additional, the camera measurements and the finite element model could be used with a more complex algorithm based on Bayesian inference to identify bridge structural parameters and imposed loading forces (Sun and Büyüköztürk 2015; Feng et al. 2015a).

Practical Considerations for Long-range Measurements

Long-range measurements introduce new challenges to video camera measurements especially due to the effects of camera motions, as small rotations manifest in large errors and apparent camera shake at range. When measuring outdoors, wind and nearby traffic (people or vehicles) can cause camera shake. To alleviate these effects a stable platform for the camera is ideal, as well as a keep out zone to prevent obvious sources of disturbances near the camera.

Since camera motion is a concern, ideally the video frame will not only include the structure under test, but some foreground and background objects that can be reasonably assumed to be mostly stationary and not vibrating at the same frequencies as the structure under test. These can be useful as references to subtract out camera motions and confirm that the frequencies measured

Chen, August 12, 2017

⁴⁷⁴ are not just due to camera shake.

⁴⁷⁵ Selection of a vantage point is relatively important to avoid as much distortion or cosine pro-
⁴⁷⁶ jection error since the camera measurement is of 3D motions projected onto the 2D image plane of
⁴⁷⁷ the camera. Ideally the camera is placed as perpendicular as possible to the primary direction of
⁴⁷⁸ the structure so there is as little cosine error as possible. This is also discussed in the limitations
⁴⁷⁹ section below.

⁴⁸⁰ **Limitations**

⁴⁸¹ The method is currently limited to relatively small motions of less than approximately 2 pixels.
⁴⁸² However, the input video can be downsampled to take larger motions and make them smaller to fit
⁴⁸³ within the bounds of acceptable amounts of motion. There are still gains even with high-resolution
⁴⁸⁴ cameras with this technique because sensor noise can be averaged out when downsampling of images
⁴⁸⁵ takes place.

⁴⁸⁶ For complex structures in situations where measuring normal to the direction of motion in the
⁴⁸⁷ image plane is not possible the projection of 3D motions or different 3D locations of the structure
⁴⁸⁸ onto the 2D image plane of the camera can represent some difficulties in accurately representing the
⁴⁸⁹ 3D motions rather than just a projection. This is out of the scope of the current paper, however it
⁴⁹⁰ is potentially possible to correct for these projections with a stereo camera setup and an accurate
⁴⁹¹ model of the camera location relative to the structure under test.

⁴⁹² Another limitation is changing lighting conditions or background conditions which can cause
⁴⁹³ apparent motions to occur in the video. Bulk changes in lighting conditions over the full scene, for
⁴⁹⁴ example due to a cloud obscuring the sun, could be taken out of the measurement by keeping track
⁴⁹⁵ of the average brightness of the full scene assuming the bulk of the scene is lit either by sunlight or
⁴⁹⁶ otherwise diffuse lighting outdoors. Also, generally these changes occur on much slower timescales
⁴⁹⁷ than the vibrations of most civil structures so they could be filtered out with a high pass filter.

⁴⁹⁸ Changing background conditions, such as clouds or other objects passing behind the structure
⁴⁹⁹ under test can also cause apparent motion. The simple method is to crop out portions of the
⁵⁰⁰ video where backgrounds conditions are adversely affecting the measurement, however this may be
⁵⁰¹ tedious. A more automatic way might be to monitor the average values of selected background

Chen, August 12, 2017

pixels to ensure there are no excess changes, which should be relatively implementable. This was not used for our measurement because the background change was not significant over the time span of our measurements.

CONCLUSION

In this paper we have conducted a comprehensive study of the WWI Memorial Bridge in Portsmouth, NH involving field measurements with a camera, a finite element model constructed directly from the plans, and a comparison and synthesis of information from both the measurement and model data. The vertical-lift bridge provides an excitation at the end of every lift that makes it easier to measure the operational resonant frequencies, which were identified at 1.7 Hz for a bending mode and 2.5 Hz for a torsional mode from the camera measurements. The camera measurements agree well with an accelerometer measurement on the bridge, and they were also combined to produce a single motion signal for a location on the bridge using a multi-rate Kalman filter data fusion algorithm. The finite element model has resonant frequencies at 1.6 Hz and 2.9 Hz that directly correlate to the bending mode and torsional mode, that are seen in a simulated lift span impact in the model. Additionally, a measurement was made of the deflection of the bridge due to traffic induced loading, and using a static load analysis in the finite element model, the weights of vehicles on the bridge were reasonably estimated from the amount of deflection measured by the camera.

Future Work

The long distance measurement already represents a significant advantage in convenience and speed over traditional sensors, however further work can greatly improve the way in which the data is collected and used. Most bridges currently have cameras to monitor traffic driving across, so this technique could be implemented on that camera feed directly. It could also be combined with traffic identification algorithms to link the specific vehicle to the induced displacement on the bridge. Multiple cameras could offer a greater variety of displacement measurement locations and could also be used to obtain some depth information on the locations of the measurement points and also potentially measure 3D motions. This would potentially alleviate errors introduced with differing scales of complex structures for pixel to physical distance calibrations as well as projections of 3D motions onto the 2D image plane of the cameras. Then the measurement locations could

be more easily correlated with nodes of a finite element model for model-based SHM applications as a stereo camera system would allow for the locations of certain pixels on a structure to be located in 3D space relative to the location of the camera. Seamless integration of the camera measurement with traditional sensor system through sensor fusion and model-based and data-driven approaches for SHM will be essential to effective measurement and decision systems for infrastructure management.

ACKNOWLEDGMENTS

REFERENCES

Bell, E. S., Lefebvre, P. J., Sanayei, M., Brenner, B., Sipple, J. D., and Peddle, J. (2013). "Objective load rating of a steel-girder bridge using structural modeling and health monitoring." *Journal of Structural Engineering*, 139(10), 1771–1779.

Boynton, B. (2014). "Ship hits new memorial bridge." *The New Hampshire Gazette* March, 7, 2014, http://www.nhgazette.com/2014/03/07/ship-hits-new-memorial-bridge/.

Caetano, E., Silva, S., and Bateira, J. (2011). "A vision system for vibration monitoring of civil engineering structures." *Experimental Techniques*, 35(4), 74–82.

Chen, J. G., Davis, A., Wadhwa, N., Durand, F., Freeman, W. T., and Büyüköztürk, O. (2016). "Video camera–based vibration measurement for civil infrastructure applications." *Journal of Infrastructure Systems*, B4016013.

Chen, J. G., Wadhwa, N., Cha, Y.-J., Durand, F., Freeman, W. T., and Buyukozturk, O. (2015).

"Modal identification of simple structures with high-speed video using motion magnification." *Journal of Sound and Vibration*, 345, 58–71.

Chen, Y., Tan, C.-A., Feng, M. Q., and Fukuda, Y. (2006). "A video assisted approach for structural health monitoring of highway bridges under normal traffic." *Smart Structures and Materials*, International Society for Optics and Photonics, 61741V–61741V.

Feng, D., Sun, H., and Feng, M. Q. (2015a). "Simultaneous identification of bridge structural parameters and vehicle loads." *Computers & Structures*, 157, 76–88.

Feng, M. Q., Fukuda, Y., Feng, D., and Mizuta, M. (2015b). "Nontarget vision sensor for remote measurement of bridge dynamic response." *Journal of Bridge Engineering*, 20(12), 04015023.

FHWA, USDOT (2012). "Moving ahead for progress in the 21st century act (MAP-21): A summary of highway provisions. July 17, 2012, http://www.fhwa.dot.gov/map21/summaryinfo.cfm.

Fleet, D. J. and Jepson, A. D. (1990). "Computation of component image velocity from local phase information." *Int. J. Comput. Vision*, 5(1), 77–104.

Fuchs, P., Washer, G., Chase, S., and Moore, M. (2004). "Laser-based instrumentation for bridge load testing." *Journal of Performance of constructed facilities*, 18(4), 213–219.

Fukuda, Y., Feng, M. Q., Narita, Y., Kaneko, S., and Tanaka, T. (2013). "Vision-based displacement sensor for monitoring dynamic response using robust object search algorithm." *IEEE Sensors Journal*, 13(12), 4725–4732.

Gautama, T. and Van Hulle, M. (2002). "A phase-based approach to the estimation of the optical flow field using spatial filtering." *Neural Networks, IEEE Transactions on*, 13(5), 1127 – 1136.

Kim, S.-W. and Kim, N.-S. (2013). "Dynamic characteristics of suspension bridge hanger cables using digital image processing." *NDT & E International*, 59, 25–33.

Lee, J. J. and Shinozuka, M. (2006). "A vision-based system for remote sensing of bridge displacement." *Ndt & E International*, 39(5), 425–431.

Lynch, J. P., Wang, Y., Loh, K. J., Yi, J.-H., and Yun, C.-B. (2006). "Performance monitoring of the geumdang bridge using a dense network of high-resolution wireless sensors." *Smart Materials and Structures*, 15(6), 1561.

Mottershead, J. and Friswell, M. (1993). "Model updating in structural dynamics: a survey." *Journal of sound and vibration*, 167(2), 347–375.

Phares, B. M., Washer, G. A., Rolander, D. D., Graybeal, B. A., and Moore, M. (2004). "Routine highway bridge inspection condition documentation accuracy and reliability." *Journal of Bridge Engineering*, 9(4), 403–413.

Pieraccini, M., Fratini, M., Parrini, F., and Atzeni, C. (2006). "Dynamic monitoring of bridges using a high-speed coherent radar." *IEEE Transactions on Geoscience and Remote Sensing*, 44(11), 3284.

Sanayei, M., Phelps, J. E., Sipple, J. D., Bell, E. S., and Brenner, B. R. (2011). "Instrumentation, nondestructive testing, and finite-element model updating for bridge evaluation using strain measurements." *Journal of bridge engineering*, 17(1), 130–138.

Smyth, A. and Wu, M. (2007). "Multi-rate kalman filtering for the data fusion of displacement and acceleration response measurements in dynamic system monitoring." *Mechanical Systems and Signal Processing*, 21(2), 706–723.

Sun, H. and Betti, R. (2015). "A hybrid optimization algorithm with bayesian inference for probabilistic model updating." *Computer-Aided Civil and Infrastructure Engineering*, 30(8), 602–619.

Sun, H. and Büyüköztürk, O. (2015). "Identification of traffic-induced nodal excitations of truss bridges through heterogeneous data fusion." *Smart Materials and Structures*, 24(7), 075032.

Sun, H. and Büyüköztürk, O. (2016). "Probabilistic updating of building models using incomplete modal data." *Mechanical Systems and Signal Processing*.

Wadhwa, N., Rubinstein, M., Durand, F., and Freeman, W. T. (2013). "Phase-based video motion processing." *ACM Trans. Graph. (Proceedings SIGGRAPH 2013)*, 32(4).

Wadhwa, N., Rubinstein, M., Durand, F., and Freeman, W. T. (2014). "Riesz pyramid for fast phase-based video magnification." *Computational Photography (ICCP), 2014 IEEE International Conference on*, IEEE.

Worden, K. (1990). "Data processing and experiment design for the restoring force surface method, part i: integration and differentiation of measured time data." *Mechanical Systems and Signal Processing*, 4(4), 295–319.

Yang, Y., Dorn, C., Mancini, T., Talken, Z., Nagarajaiah, S., Kenyon, G., Farrar, C., and Mascareñas, D. (2017). "Blind identification of full-field vibration modes of output-only structures from uniformly-sampled, possibly temporally-aliased (sub-nyquist), video measurements." *Jour-*

615   *nal of Sound and Vibration*, 390, 232–256.

616   Yuen, K.-V. and Kuok, S.-C. (2011). "Bayesian methods for updating dynamic models." *Applied*

617   *Mechanics Reviews*, 64(1), 010802.

618   Zhou, Y. E. (2006). "Assessment of bridge remaining fatigue life through field strain measurement."

619   *Journal of Bridge Engineering*, 11(6), 737–744.

Chen, August 12, 2017